A Novel Exoskeleton Neuromuscular Interface Based on Motor Unit Action Potential Model Using High-Density sEMG

Weibo Wang, Long He, Jian Wang, Min Pan, Jingang Yi, Ningtao Cheng, and Tao Liu

***Abstract*—The topical and noninvasive measurement of high-density surface electromyogram (HD-sEMG) signals enables the estimation of human motor unit action potentials (MUAPs) as important motor function indicators for human-robot interaction. In this paper, a two-dimensional (2D) high-density micro-needle electrode array is developed using the KOH bulk etching technique and the flexible printed circuit (FPC). To determine the optimal configuration of the 2D electrode array, an accurate and efficient neuromuscular analytical model for HD-sEMG is proposed to comprehensively analyze the effects of the micro-needle electrode size, inter-electrode distance, and location. The elbow joint angle estimation experiment for the sEMG-based upper-limb exoskeleton has further been conducted to demonstrate the feasibility and performance of the proposed micro-needle-based high-density electrode array, which is compared with a commercial wet electrode. The experimental results showed that the proposed micro-needle electrode with high spatial resolution was comparable to the wet electrode (Wilcoxon rank sum test, $p > 0.05$). On average, the correlation and root mean squared error (RMSE) of the micro-needle electrode array with high space utilization were 7.56% and 19.83% better than those of the wet electrode, respectively. The 2D high-density micro-needle electrode array based on the proposed HD-sEMG model facilitates a novel neural-machine interface for intuitive control of upper-limb exoskeletons.**

***Index Terms*—HD-sEMG modeling, high-density, micro-needle electrode array, motor unit, electrode configuration.**

I. Introduction

SURFACE electromyogram (sEMG) contains the action potentials of motor units (MUs) and has been widely used in many fields, such as medical rehabilitation, competitive sports, and human-robot interaction [1]–[3]. High-density surface electromyogram (HD-sEMG) uses multiple closely spaced electrodes overlying a restricted area of the skin to measure human motor unit action potentials (MUAPs) [4].

The main challenges of high-quality sEMG acquisition are the high impedance of the skin stratum corneum and motion artifacts [5]. The conductive gel in the conventional wet electrode not only significantly reduces the electrode-skin contact impedance, but also has good adhesion. Limited by the small electrode area, the HD-sEMG sensors use rigid dry electrodes and have poor performance [6]. The micro-needle electrodes have made great progress in materials, structures, and fabrication methods [7]. The introduction of micro-needles into HD-sEMG sensors will address these challenges. The micro-needles can penetrate the skin stratum corneum and avoid electrode displacement [5]. A majority of studies focus on skin-like, soft, and stretchable properties of sensors [8], [9], however, few of them have considered the high-density and multi-channel properties and electrode configuration (e.g., electrode size, inter-electrode distance, and placement). The electrode configuration greatly affects the accuracy of the application [10]–[13].

Although a common body of knowledge has been established through publication [14], many of its recommendations are statistical summaries and not applicable to HD-sEMG sensor configuration. The neuromuscular analytical model provides an outlet for interpreting and simulating sEMG signals [15], [16], sEMG filtering [17], and neuropathological diagnosis [18]. Furthermore, it provides a simulation method for electrode configuration [19], such as monopolar and bipolar electrodes. In [20], the effects of electrode size and inter-electrode spacing on the detection distance were examined using an approximate method. The work in [21] proposed a two-dimensional (2D) spatial filtering technique without approximation of the integration effect and restriction of electrode shapes. It has been noted that monopolar, bipolar, and Laplacian electrode configurations affect the accuracy of force level classification in simulation and experimental studies [10], [11]. However, with the development of HD-sEMG, the implication of a 2D electrode array composed of monopolar and bipolar montages in HD-sEMG imaging deserves specific attention [22], [23].

Existing analytical models have two drawbacks to be solved for HD-sEMG. First, most of them consider single fiber action potentials (SFAPs) recorded by a single electrode [24], [25], or MUAPs [20], [26]. Those models are limited by the complex anatomical structure of the muscle and at high computational

This work was supported in part by the National Natural Science Foundation of China (NSFC) under Award 52175033, U21A20120, and 82202628, in part by the Zhejiang Provincial Natural Science Foundation under Award LZ20E050002, in part by the Key Research and Development Programme of Zhejiang under Grant 2023C03196, 2022C03103, and 2021C03051. (*Corresponding author: Tao Liu*)

W. Wang and T. Liu are with the State Key Laboratory of Fluid Power and Mechatronic Systems, School of Mechanical Engineering, Zhejiang University, 310027, Hangzhou, China (e-mail: 12025019@zju.edu.cn; liutao@zju.edu.cn).

L. He is with the School of Mechanical Engineering, Nanjing University of Science and Technology, Nanjing, China (e-mail: helong_zyy@163.com).

J. Wang is the director of Sports and Health Engineering Institute, School of Education, Zhejiang University, 310058, Hangzhou, China (e-mail: pclabeeg@zju.edu.cn).

M. Pan is a reader in the Department of Mechanical Engineering, University of Bath, BA2 7AY Bath, UK (e-mail: mp351@bath.ac.uk).

J. Yi is with the Department of Mechanical and Aerospace Engineering, Rutgers University, Piscataway, NJ 08854 USA (e-mail: jgyi@rutgers.edu).

N. Cheng is with the School of Medicine, Zhejiang University, 310058, Hangzhou, China (e-mail: ncheng@zju.edu.cn).

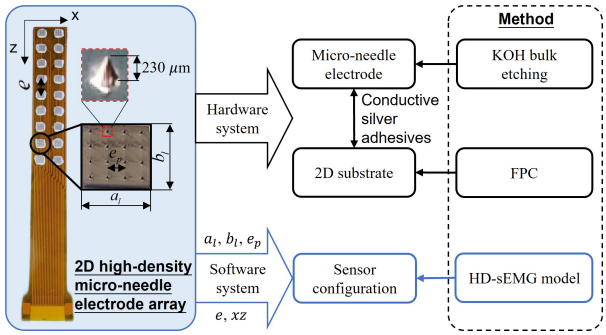

Fig. 1. Schematic diagram of the novel exoskeleton neuromuscular interface.

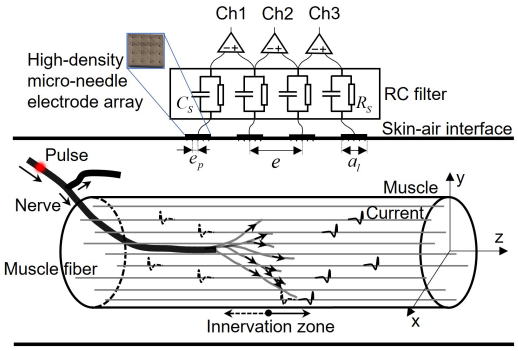

Fig. 2. Illustrative diagram of the HD-sEMG model development.

costs. However, the computational costs are unaffordable for configurations with tens to hundreds of electrodes [15], as shown in Table S1 in the supplementary material. A few studies discussed approaches to reduce the computation time, such as the notion of the isopotential layer [20] and the principle of reciprocity [27]. The work in [15] reduced the computation time by setting all the computations in a 3D Fourier domain and using parallel computing. Built on [15], the work in [28] presented a method of macro-scale motor unit electrical source, which was 10% more efficient than parallel computing. However, the simulation efficiency is unsatisfactory when the muscle fiber orientation and curvature are considered or additional MUs are recruited [27]. Moreover, the SFAP and MUAP models neglect the interaction and comprehensive effects of muscle fibers and MUs and therefore cannot be applied to HD-sEMG applications [28]. Second, while they minimally influence the single-channel recordings, specific characteristics have substantial effects on the multi-channel results, particularly the MU territory locations in the muscle cross-section and the motor end-plate geometry [26].

In this paper, we present a 2D high-density micro-needle electrode array with high spatial resolution and high space utilization. The proposed micro-needle electrode is fabricated from silicon by the KOH bulk etching technique and integrated with a flexible printed circuit board (FPC). An accurate and efficient neuromuscular analytical model for HD-sEMG is proposed to simulate the micro-needle electrode size, inter-electrode distance, and location of the 2D electrode array for optimal sensor configuration. In our model, we consider a cylindrical muscle, with all muscle fibers parallel to the axis of the muscle; see Fig. 2. A neighborhood judgment algorithm (NJA) is proposed to uniformly locate the MU territory and muscle fiber in the muscle cross-section. The motor end-plates of MU are modeled as a multi-band Gaussian distribution. These new features are appropriate for multi-channel recordings. Based on the uniformity of muscle fibers and multi-band distribution of motor end-plates, a simplified computational method for MUAP generation is proposed to reduce the computational time. The elbow joint angle estimation experiment for the sEMG-based upper-limb exoskeleton was performed, and the performance of the micro-needle-based high-density electrode array was verified by comparing it with the conventional wet electrode.

The main contributions of the work are twofold. First, a 2D high-density micro-needle electrode array with high spatial resolution and high space utilization is designed, which has the promising potential for neural-driven-based applications. Second, we present an accurate and efficient neuromuscular analytical model for HD-sEMG sensor configuration. We optimize the modeling of MU location, muscle fiber location, and motor end-plate distribution for multi-channel recordings. The uniformity of the location is in good agreement with the expected data (21.08 ± 1.22 compared with 20.79 fibers/mm^2). The simplified MUAP computational method leads to a six-fold reduction in the computation time of the HD-sEMG, from 1 hour in other methods to 10 mins in this work.

II. Materials and Methods

A. 2D High-Density Micro-Needle Electrode Array

As shown in Fig. 1, we developed a 9×2 high-density micro-needle electrode array for the sEMG-based upper-limb exoskeleton control.

1) Hardware System: The 2D electrode array consists of two main components: micro-needle electrodes and a 2D flexible substrate. Silicon has good biocompatibility, chemical stability, and high hardness, which can penetrate the skin stratum corneum and achieve long-term sEMG monitoring. The noninvasive silicon micro-needle electrode with a height of 230 μm is fabricated by the KOH bulk etching technique. It is then sputtered with a layer of silver with a thickness of 200 nm and finally integrated with the FPC using conductive silver adhesives (Ablebond 84-1LMISR4, Germany).

2) Software System: The 2D electrode array is characterized by five parameters, including the size $a_l \times b_l$ and the inter-electrode distance e of the micro-needle electrode, the pin-to-pin distance e_p of the micro-needle, and the layout (e.g., 9×2) in the xz-plane. In addition to its characteristics, the configuration of the sensor also includes the location on the skin and the maximum limit of size. An accurate and efficient neuromuscular analytical model for HD-sEMG (HD-sEMG model in Section II-B) is used to determine the optimal sensor configuration, which is described in Section II-C.

B. HD-sEMG Model

Fig. 2 illustrates the basic modeling setup for HD-sEMG. The Cartesian coordinates are fixed on the muscle center with the z-axis parallel to the muscle fiber direction, and the xy-plane is the muscle cross-section. The muscle is surrounded

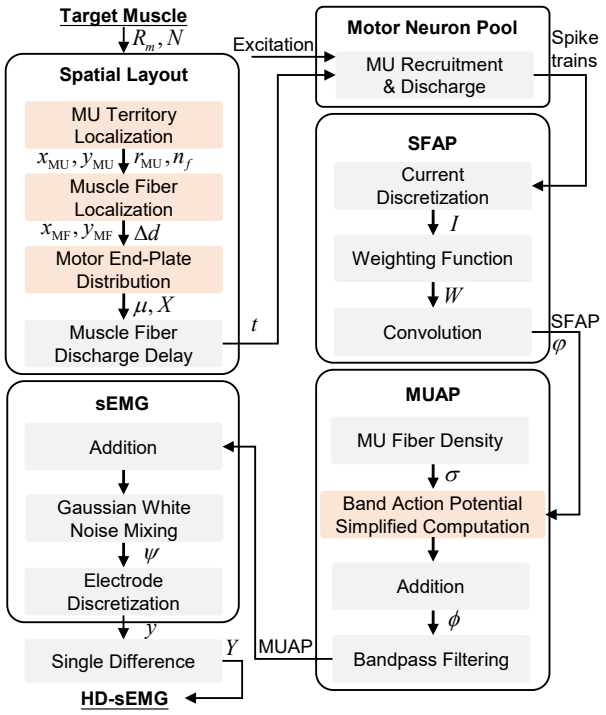

Fig. 3. Flowchart diagram of the HD-sEMG model development. x_{MU} and y_{MU} are the x- and y-coordinate of the MU, and x_{MF} and y_{MF} are the x- and y-coordinate of the muscle fiber, respectively.

by skin and fat tissues whose behaviors are modeled by a RC filter. Pulses from the nerve conduct in both directions along muscle fibers. The potentials detected by the high-density micro-needle electrode array are filtered and amplified.

Fig. 3 shows the flowchart diagram of the HD-sEMG modeling approach. We highlight the main new developments in the figure, that is, the locations of MU territory and muscle fiber, the distribution of motor end-plate, and the simplified computation of MUAP generation. The modeling approach comprises five modules: spatial layout, motor neuron pool, SFAP, MUAP, and sEMG. The spatial layout module establishes an equivalent virtual muscle model and describes the modeling methods of MUs, muscle fibers, and motor end-plates for multi-channel recordings. The motor neuron pool module defines how each MU is recruited and the relationship between the excitation and discharge after recruitment. The remaining three modules describe the modeling methods of SFAP, MUAP, and sEMG after the muscle established in the first module is activated by the second module. In the following, we describe these modules and mainly highlight the newly developed components.

1) Uniform distribution of MU territory centers: The MU territory centers are evenly covered throughout the muscle cross-section based on the experimental study of [29]. We propose the NJA algorithm that makes the position of the MU territory center quasi-random, that is, not limited by a fixed layout and the initial point position. The goal of the NJA algorithm is to generate uniformly distributed MU territory centers at a low time cost.

We assume that the muscle cross-section located at (x_c, y_c) is a circular shape with a known radius R_m and the total

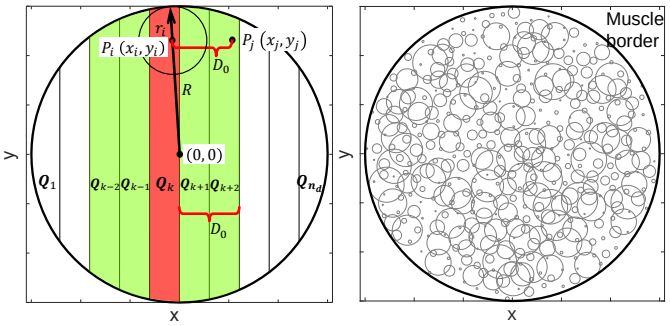

Fig. 4. (a) Illustrative schematic of the NJA algorithm. The red region represents the set where the newly generated point is located, and the green regions represent the sets that need to be calculated. (b) Distribution of $N = 443$ MUs across the muscle cross-section. The circles within the muscle border are the MU boundaries.

number of MUs is N. The desired distance d_0 between two adjacent points in the grid layout is calculated by estimating the number of points distributed over the radius with formula fitting. The NJA algorithm is to calculate the Euclidean distance between the newly generated point and the existing points in turn. If the distance is greater than or equal to d_0, the point is retained; otherwise, it is discarded. Then the next new point is generated randomly until the number of retained points reaches N. The optimization of this algorithm is to reduce the calculation when experiencing a number of points. In fact, only points close to this new point will be calculated.

As shown in Fig. 4a, starting from the origin $(0, 0)$, the entire muscle cross-section is divided into n_d sets by vertical lines that are spaced by $D_0/2$ apart, where $D_0 = d_0/\epsilon$ and constant $\epsilon > 1$ is chosen to compromise the computational cost and distribution uniformity. The sets are denoted as $\boldsymbol{Q}_l$, $l = 1, \ldots, n_d$. As an example, a given point P_i falls in $\boldsymbol{Q}_k$, and it just needs to calculate the Euclidean distance between it and the existing points in $\boldsymbol{Q}_k$, $\boldsymbol{Q}_{k-1}$, $\boldsymbol{Q}_{k-2}$, $\boldsymbol{Q}_{k+1}$, and $\boldsymbol{Q}_{k+2}$. The MU is usually defined as a circular territory with a certain radius [20], [28]. Therefore, the NJA algorithm needs to ensure that not only the MU territory center but also the entire territory is located within the muscle cross-section. Fig. 4b shows an example of the distribution of MUs across the muscle cross-section by the NJA algorithm. The circles within the muscle border are the MU boundaries. Algorithm 1 further illustrates the outline of the NJA algorithm for uniformly distributed points.

The distribution of muscle fibers in a MU is also confirmed to be uniform [30]. We denote the generated MU_i territory center as $(x^i_{\mathrm{MU}}, y^i_{\mathrm{MU}})$, the radius as r^i_{MU}, the total number of muscle fibers as n^i_f, and the muscle fiber diameter as d^i_f. The uniform location layout can also be obtained by the NJA algorithm.

2) Multi-band Gaussian distribution of motor end-plates: The physiological structure on the muscle fiber where the excitation occurs is called the motor end-plate. The motor end-plate position (the z-axis coordinate) varies in different bands of the MU territory. The band division of each MU territory in the muscle cross-section is based on two principles: (1) *Proximity principle*: Within the same MU, adjacent muscle

Algorithm 1: The NJA algorithm

Input : Center (x_c, y_c), R, N, radii $\boldsymbol{r} = \{r_i\}$
Output: $(\boldsymbol{x}, \boldsymbol{y})$

$n = \frac{1+\sqrt{N-4}}{2}$, $d_0 = \frac{R}{\lceil n \rceil}$, and $D_0 = d_0/\epsilon$, $i \leftarrow 1$;
Partition cross-section into n_d regions with $\boldsymbol{Q}_l = \varnothing$, $l = 1, \ldots, n_d$;
while $i \leq N$ **do**
  Randomly generate $P_i = (x_i, y_i)$, $x_i, y_i \in [-R, R]$;
  if $|P_i| \leq R - r_i$ **then**
    $k = \left\lfloor \frac{x_i}{D_0/2} \right\rfloor + \left\lceil \frac{R}{D_0/2} \right\rceil + 1$, $\boldsymbol{\psi} = \varnothing$;
    $\boldsymbol{\psi} \leftarrow \boldsymbol{Q}_{k-2} \cup \boldsymbol{Q}_{k-1} \cup \boldsymbol{Q}_k \cup \boldsymbol{Q}_{k+1} \cup \boldsymbol{Q}_{k+2}$;
    if $\forall P_j \in \boldsymbol{\psi}, |P_i P_j| \geq D_0$ **then**
      $\boldsymbol{Q}_k \leftarrow \boldsymbol{Q}_k \cup \{P_i\}$;
      $(\boldsymbol{x}, \boldsymbol{y}) \leftarrow (\boldsymbol{x}, \boldsymbol{y}) \cup \{(x_i + x_c, y_i + y_c)\}$;
      $i \leftarrow i + 1$;

fibers have similar properties such as length and motor end-plate position. Based on this, we divide the muscle fibers in the neighborhood into a band. (2) *Simplified calculation principle*: The band division needs the reference and proximity distance. Since the action potential is highly related to the distance between the electrode and the muscle fiber, we take the position of the electrode ($x = 0$) as the reference and the safe distance (e.g., 0.5 mm) that does not affect action potentials as the width of each band to simplify the calculation of action potentials [20].

Fig. 5 illustrates the motor end-plate band division for a given MU_i, $i \in \mathbb{N}$. The reference point is at location $x = 0$. Centered at the reference point, a set of equally-distanced arc-shaped dotted lines are crossing MU_i, and a band is formed between two adjacent dotted lines with band width Δd. The average motor end-plate position μ_i for MU_i is assumed to be Gaussian distributed with a mean of 0 and a standard deviation of σ_{MU}. The motor end-plate position X_i^j of the jth band in MU_i also satisfies the Gaussian distribution and is expressed as

$$X_i^j \sim \mathcal{N}\left(\mu_i, \sigma_b^2\right), \ -L_0/2 \leq X_i^j \leq L_0/2, \tag{1}$$

where σ_b is the standard deviation, $\sigma_b < \sigma_{\text{MU}}$, $j = 1, \ldots, n_b$, n_b is the number of bands crossing MU_i, and L_0 is the range of motor end-plate position.

3) Discharge delay of muscle fibers: Due to differences in the conduction path and conduction velocity among muscle fibers, the same excitation arrives at motor end-plates at different times, resulting in delayed discharges of muscle fibers. The muscle fiber discharge delay t_{ij} at the jth band in MU_i can be expressed as

$$t_{ij} = t_i + t_{bi}^j, \tag{2}$$

where t_i and t_{bi}^j represent the delays of MU_i among MUs and the jth band among bands in MU_i, respectively, and are calculated as

$$t_i = \frac{\mu_i - \min(\mu_i)}{v_f}, \ t_{bi}^j = \frac{|X_i^j - \mu_i|}{v_p}, \tag{3}$$

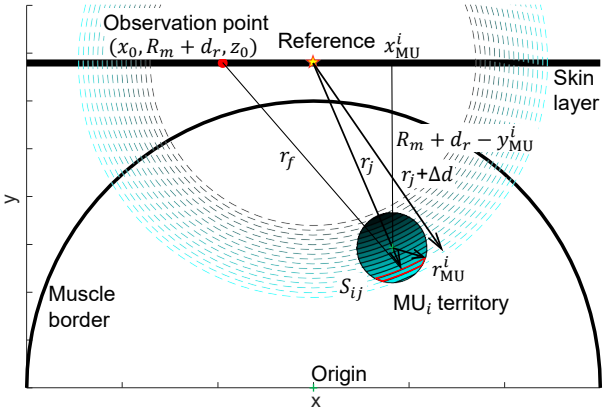

Fig. 5. Illustrative schematic of the motor end-plate band division on the muscle cross-section. Centered at the reference point, each band is filled with the same color as indicated by the arc-shaped dotted line. The darker the color, the greater the contribution of action potentials generated by the current source within the band.

and v_f and v_p are the conduction velocities of axons and telodendrias of motor neurons, respectively.

When the excitation in the trigger zone reaches the recruitment threshold of a MU, the motor neuron of this MU starts to fire at a minimum firing rate (MFR). Due to the relation between stimulus rate and isometric force for MUs, the peak firing rate (PFR) for MU_i is calculated as $\text{PFR}_i = 1.5/T_i$, where T_i is the contraction time of MU_i. The recruitment threshold excitation (RTE) and the contraction time of MU_i are distributed according to the principle in [31]. The linear gain g_e of the excitation-firing rate relationship is calculated as $g_e = \frac{\text{PFR}_N - \text{MFR}}{100 - \text{RTE}_N}$. The spike trains of MU_i are obtained with a coefficient of variation of 0.2 in the interspike intervals and t_{ij} added to them.

4) SFAP modeling: Under the premise of a time shift-invariant system, SFAP φ_{ij} at the jth band in MU_i can be expressed as the discrete convolution of the current source I and the weighting function W of the volume conductor system [27], [32], [33], namely,

$$\varphi_{ij}(k, x_0, z_0) = \sum_{l=0}^{n_t - 1} I_i(l) W_{ij}(k_t, x_0, z_0), \tag{4}$$

where $k_t = kt_s - t_{ij} - l\Delta t$, $k \in \mathbb{N}$, $t_s = 1/f_s$ is the sampling interval, $I_i(l)$ is derived from the trans-membrane current source proposed in [34] and discretized at intervals of Δt for MU_i [32], $l = 0, \ldots, n_t - 1$ is the serial number of the pulse of the current source, and n_t is the total number of pulses. The weighting function W captures the effect of the current source on the muscle fiber, and at the kth sampling time, it is calculated as

$$W_{ij}(k_t, x_0, z_0) = \frac{1}{4\pi\sigma_r \sqrt{r_f^2 \frac{\sigma_z}{\sigma_r} + (av_i k_t + X_i^j - z_0)^2}}, \tag{5}$$

where $a = -1$ or 1 when the current source is on the left- or right-half muscle fiber, respectively. σ_r and σ_z are the transversal and longitudinal muscle tissue conductivity, respectively, and v_i is the conduction velocity of the muscle fiber in MU_i. r_f is the distance between the observation point at $(x_0, R_m + d_r, z_0)$ and the muscle fiber. d_r is the tissue (skin

and fat) thickness. As shown in Fig. 5, the distance r_j of the muscle fiber in the jth band to the reference point and the area S_{ij} of the jth band in MU$_i$ can be obtained by arithmetic geometry.

5) MUAP modeling: MUAP is calculated by adding the SFAPs of all muscle fibers belonging to the same MU [35]. To reduce the computation, we propose a simplified MUAP computational method using the multi-band distribution of motor end-plates and the uniform distribution of muscle fibers. By doing so, we only need to calculate one SFAP in each band and then multiply the number of muscle fibers contained in this band (i.e., band area multiplied by MU fiber density). MUAP ϕ_i for MU$_i$ is the sum of the action potentials produced by all bands, and at (x_0, z_0) and the kth step, it is calculated as

$$\phi_i(k, x_0, z_0) = \sum_{j=1}^{n_b} \varphi_{ij}(k, x_0, z_0) S_{ij} \sigma, \tag{6}$$

where σ is the MU fiber density. Both skin and fat show distinctive capacitive behavior except for resistive behavior [6]. In this work, the MUAP is passed through a second-order Butterworth bandpass filter with low and high frequency cut-offs of 10 Hz and 450 Hz to simulate those behaviors of skin and fat and retain effective components [36].

6) HD-sEMG modeling: sEMG ψ observed at a point is the sum of MUAPs of all recruited MUs with added Gaussian white noise [27], [36]. The sEMG signal observed by the electrode is equivalent to the average of the sEMG at each point across its surface [20], [26]. The HD-sEMG signal $\boldsymbol{Y} \in \mathbb{R}^{m \times n}$ observed by the electrode grid $(m+1) \times n$ at the kth step is given by $\boldsymbol{Y}(k) = [\boldsymbol{Y}_1(k) \ \cdots \ \boldsymbol{Y}_n(k)]$,

$$\boldsymbol{Y}_j(k) = \left[y_{1j}(k) - y_{0j}(k) \ \cdots \ y_{mj}(k) - y_{(m-1)j}(k) \right]^T \tag{7}$$

where $y_{ij}(k)$ is the sEMG measurement at the kth step by the $(i+1)$th row and the jth column electrode, $i = 0, \cdots, m$, $j = 1, \cdots, n$, and $\boldsymbol{Y}_j$ is the jth sEMG array with m elements. Algorithm 2 further illustrates the outline of the proposed HD-sEMG model.

Algorithm 2: The HD-sEMG model-based computation

Input : $\boldsymbol{I}$, R_m, N, $\boldsymbol{n_f} = \{n_f^i\}$, $\boldsymbol{d_f} = \{d_f^i\}$, $\boldsymbol{v} = \{v_i\}$, σ, MFR, $\boldsymbol{\mathrm{RTE}} = \{\mathrm{RTE}_i\}$, $\boldsymbol{T} = \{T_i\}$

Output: $\boldsymbol{Y}$

for $i \leq N$ **do**

- Compute r_{MU}^i with n_f^i of MU$_i$;
- Locate MU$_i$ using the NJA with $(0,0), R_m, N, r_{\mathrm{MU}}^i$;
- Locate muscle fibers for MU$_i$ using the NJA with $(x_{\mathrm{MU}}^i, y_{\mathrm{MU}}^i), r_{\mathrm{MU}}^i, n_f^i, \frac{d_f^i}{2}$;
- Divide MU$_i$ into n_b bands;
- Activate MU$_i$ with g_e and obtain the spike train;
- **for** $j \leq n_b$ **do**
  - Compute X_i^j by (1) and t_{ij} by (2) and (3);
  - Update the spike trains with t_{ij};
  - Compute $\varphi_{ij}(k, x_0, z_0)$ by (4) and (5);
- Compute $\phi_i(k, x_0, z_0)$ by (6);
- Update ϕ_i with a Butterworth filter and $\psi \leftarrow \psi + \phi_i$;

Update ψ with Gaussian white noise;

Compute $\{y_{ij}\}$ and $\boldsymbol{Y}$ by (7);

TABLE I
THE VALUES OF THE MODEL PARAMETERS

Model Parameter (unit)	Symbol	Values
Muscle fiber length (mm)	L	80 [32]
Muscle radius (mm)	R_m	13 [32]
Muscle fiber number	N_0	30606 [28]
MU number	N	120 [31]
Recruit. threshold excitat. (% MVC)	RTE	1-80 [31]
MU fiber number	n_f	21-1720 [31]
MU fiber density (fibers/mm^2)	σ	20.79 [31]
Tissue (skin and fat) thickness (mm)	d_r	4 [32]
Muscle tissue conductivity (z) (S/m)	σ_z	0.33 [25]
Muscle tissue conductivity (xy) (S/m)	σ_r	0.063 [25]
Peak firing rate (pulses/s)	PFR	15-37.5 [31]
Minimum firing rate (pulses/s)	MFR	8 [31]
MU fiber diameter (μm)	d_f	16-75 [37]
Motor end-plate range (mm)	L_0	5 [38]
Conduction velocity (m/s)	v	2.5-5.5 [37]
Sampling frequency (Hz)	f_s	1000 [37]

C. Sensor Configuration Based on the HD-sEMG Model

Table I shows the model parameters used for the sensor configuration.

1) Simulation of the electrode size: We simulated several commonly used sizes of square electrodes, that is, 1×1, 3×3, 4×4, 5×5, and 10×10 mm. The electrodes were placed at $(0, R_m + d_r, 0)$ in each simulation and were approximated by $n \times n$ points, $n = 3, 7, 9, 11, 21, 51$. The effect of the electrode size was assessed with the average rectified value (ARV) of the MUAP measured by the electrode [39].

2) Simulation of the inter-electrode distance: The inter-electrode distance e is the spatial sampling of the signal, and the spatial sampling frequency $x_s = v/f_s$ [22], [32], [35]. Therefore, the range of the spatial sampling frequency mainly depends on the range of conduction velocities of muscle fibers (2.5-5.5 m/s) when the sampling frequency f_s is set to the minimum value of 1000 Hz, which brings a challenge of the miniaturized design of electrodes. We simulated the inter-electrode distance of $2.5, 3.5, 4.5, 5.5, 10, 15$, and 20 mm, with one electrode placed at $(0, R_m + d_r, 5)$. The effect of the inter-electrode distance was assessed with the ARV, median frequency (MNF), and mean power frequency (MPF) of the MUAP [20].

Detection volume is an important factor for the sEMG measurement, and the discussion in Section II-B1 is closely related to the detection volume. The randomness of the MU position in the muscle cross-section directly leads to different results for each simulated sEMG. Thus, referring to (6), we built a MUAP model to study the amplitude and frequency contributions of the MU to the sEMG signal when it was located at different depths along the y-axis direction. The

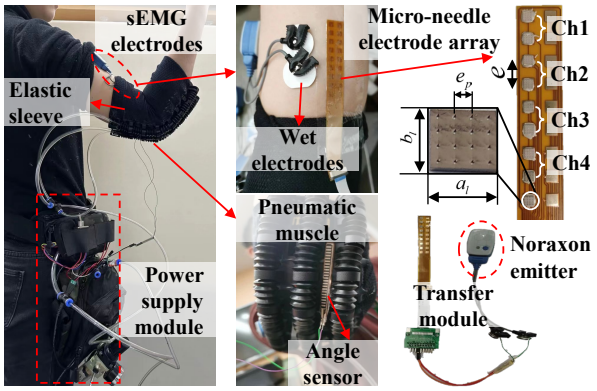

Fig. 6. Human subject experimental setup for elbow joint angle estimation.

depth away from the electrode $(0, R_m + d_r, 0)$ ranges from 5 to 11 mm with 1 mm increments.

3) Simulation of the electrode location: During movement, the muscles slide with respect to the skin, and this relative motion contributes to geometrical artifacts. The innervation zone should be located, and the electrodes should not be placed near it to avoid artifacts. In this section, we identify the innervation zone by scanning and thus determining the appropriate electrode location. We take one MU with the xy-coordinate at $(0.80, 10.56)$ mm as the example to demonstrate the application. The MU radius is $r_{\text{MU}} = 0.214$ mm, and the range of the innervation zone is $[0.4659, 0.4678]$ mm. We take scanning intervals of 1 mm along the positive and negative directions of the z- and x-axis for the localization of the innervation zone and MU territory. The location of the innervation zone can be estimated from the differential signals because of the minimum value of ARVs along the array and the detectable phase reversal [27], [39]. The signals obtained at adjacent scan positions are differentiated, and the differential signals are normalized with the peak-to-peak value of the signal obtained at $(0, R_m + d_r, 0)$.

D. Electrode Experiment for Elbow Joint Angle Estimation

After the 2D high-density micro-needle electrode array is designed, it is necessary to evaluate the signal acquisition performance of the proposed electrode. The elbow joint angle estimation experiment for the sEMG-based upper-limb exoskeleton was conducted, and the performance of the proposed electrode array was verified in comparison with commercial wet electrodes.

1) Experimental preparation: Six healthy subjects (five males and one female; age: 24.7 ± 2.7 years; height: 168.6 ± 3.6 cm; weight: 60.3 ± 5.4 kg) with no history of neuromuscular disorders gave written informed consent before participating in the experiment. This study was approved by the Medical Ethics Committee of the School of Biomedical Engineering and Instrument Science, Zhejiang University (Project identification code: 2021 - 39).

sEMG signals of the biceps brachii muscle were recorded simultaneously with the proposed high-density micro-needle electrode array and a pair of commercial wet electrodes (22 mm in diameter and 20 mm in spacing) at a sampling frequency of 2000 Hz (Ultium, Noraxon Inc., USA). As shown in Fig. 6, they were symmetrically arranged in the muscle belly. The electrode array was connected to the emitter (Ultium, Noraxon Inc., USA) by a self-made transfer module. True angle was measured synchronously by a strain gauge angle sensor (Flex, Crownto Electronic Technology Ltd., China) on the pneumatic muscle of our self-made upper-limb exoskeleton and sampled at 100 Hz. The pneumatic muscle was tightly attached to the back of the elbow with elastic sleeves.

2) Experimental procedure: During the experiment, the upper-limb exoskeleton had no power supply. The subjects were required to perform elbow flexion and extension as uniformly as possible at a speed of no more than 1 Hz under three load conditions of 0 kg, 0.5 kg, and 1 kg. In each condition, the subject held a dumbbell of the corresponding weight and repeated the elbow flexion and extension movement 5 times.

3) Data processing: The raw sEMG signals were first filtered between 30 and 450 Hz using a second-order Butterworth bandpass filter and further filtered the powerline interference at 50 Hz and its harmonics using the notch filter with a cut-off bandwidth of 4 Hz [1], [2], [40]. The angle was interpolated to meet the synchronization with sEMG. We set data windows of 200 ms in 50 ms increments, which is considered appropriate to meet real-time requirements [4], [40]. In each window, the root mean square (RMS) feature of the sEMG and the mean feature of the angle were extracted [1], [2], [40]. Fivefold cross-validation was used to divide the training and testing data. The back-propagation neural network (BPNN) including three layers was used to estimate the elbow joint angle, which was widely used in previous studies [2]. The training data from each load trained one BPNN. The input to the BPNN was the RMS feature of the sEMG. The number of nodes in the input and output layers depends on the number of channels of the sEMG and angle, respectively. We set different numbers of nodes (from 3 to 12) in the hidden layer to select the best structure of the BPNN. The sigmoid activation function is chosen in the network training. The agreement between the estimated and true angles was quantitatively examined using the correlation and root mean squared error (RMSE).

III. Results

In this section, we first present the HD-sEMG model validation, then demonstrate applications of the model in optimizing the sensor configuration, and finally demonstrate the angle estimation accuracy of the proposed 2D electrode array compared with wet electrodes.

A. Model Validation and Performance Demonstration

Ensuring the uniformity of muscle fibers is one of the requirements for the simplified computational method of MUAP generation. Fig. 7 shows a typical result of the band division and the uniform distribution of muscle fibers within one MU. The black numbers represent the actual number of muscle fibers generated in each band, and the red numbers represent the absolute difference between the expected number and the actual number of muscle fibers in each band. The average value of these red numbers is 2.3, with a maximum of 6.98. The maximum value accounts for 9.56% of the expected

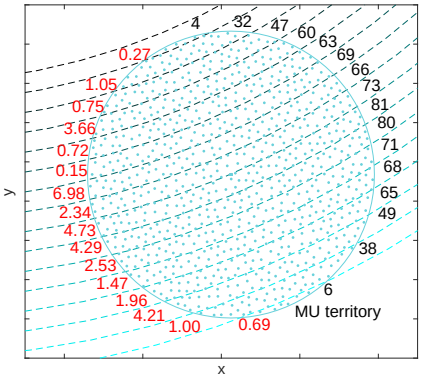

Fig. 7. A typical result of the band division and the uniform distribution of muscle fibers within one MU. The total number of muscle fibers innervated by the MU is 872. Note that the expected number of muscle fibers (band area multiplied by the MU fiber density σ) is not an integer.

TABLE II
COMPUTATION TIME WITH AND WITHOUT SIMPLIFICATION

	Case 1 (s)	Case 2 (s)	NRMSE (%)
MUAP	30.3 ± 15.8	123.3 ± 9.7	0.48 ± 0.41
sEMG	136.3 ± 11.5	3929.5 ± 544.2	3.37 ± 0.07

number of the corresponding band. The actual MU fiber density is 21.08 ± 1.22 fibers/mm^2 ($\sigma = 20.79$ fibers/mm^2).

To evaluate the computational cost, we simulated the MUAP of one MU (see Fig. 7) and a single-channel sEMG with (case 1) and without (case 2) the proposed simplified MUAP computational method. Each case was executed three times, and a representative example of the simulated sEMG in case 1 was shown in Fig. S1 in the supplementary material. Table II lists the average computation time. We also computed the normalized root mean squared error (NRMSE) between the signals generated in the two cases to ensure consistency between the signals. The NRMSE of the MUAP was averaged across all MUs. With the proposed method, the errors are 0.5% and 3.5% on the MUAPs and the sEMG, respectively. The computation times are reduced by 75.4% and 96.5% for the MUAP and the sEMG, respectively. The computation time is greatly reduced without sacrificing the simulation accuracy, with the average computation time of a single-channel sEMG being less than 3 mins. Furthermore, the representative computation time for HD-sEMG on an 8×8 electrode grid simulated with the proposed computational method is less than 10 mins.

B. Sensor Configuration Based on the HD-sEMG Model

1) Effects of the electrode size: Fig. 8 shows the ARV values that were normalized by the value at the electrode center. A larger n results in a more accurate ARV value; therefore, the ARV when $n = 51$ is taken as the estimate of the actual ARV of the electrode. We then calculated the 90% confidence interval of the actual ARV, and the n corresponding to the ARV outside the confidence interval is regarded as a false approximation to the electrode. The calculation concludes that the cases of $n \geq 9$ approximate the electrodes well. Correspondingly, the distance between points does not exceed

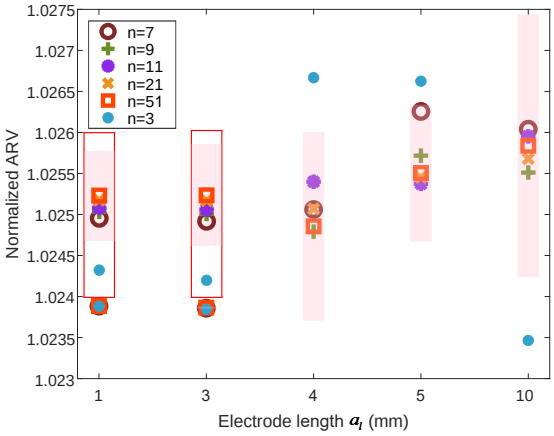

Fig. 8. The normalized ARV of one MU from electrodes with different sizes. The calculated ARV was normalized by the value calculated at the electrode center. The pink-filled area represents the 90% confidence interval. Shown in the two red boxes are enlarged images of the results for electrodes of size of 1 and 9 mm^2.

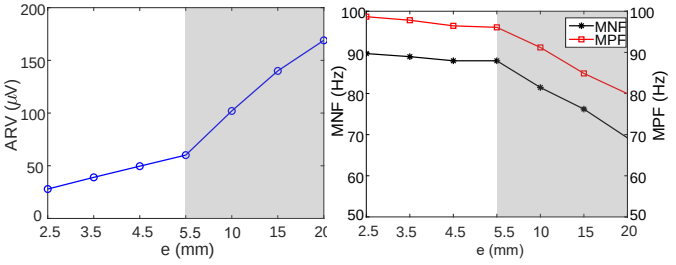

(a) (b)

Fig. 9. The ARV, MNF, and MPF values as a function of the inter-electrode distance. The inter-electrode distance is taken from 2.5 to 5.5 mm with 1 mm increments. The shaded area shows the results of the commonly used inter-electrode distance.

1.25 mm, and this guides the design of the pin-to-pin distance e_p of the micro-needle electrode.

2) Effects of the inter-electrode distance: Fig. 9 shows the computed ARV, MNF, and MPF values over varying inter-electrode distances. The ARV values increase with larger inter-electrode distances, while the MNF and MPF values decrease.

Fig. 10 shows the MUAP aptitude profiles in the time and frequency domains under different MU depths. When the MU is located deeper in the muscle, the generated MUAP has a smaller amplitude. In the frequency domain, with increased depths, the MUAP signal's high-frequency components gradually disappear, and the amplitude of each frequency component reduces as well.

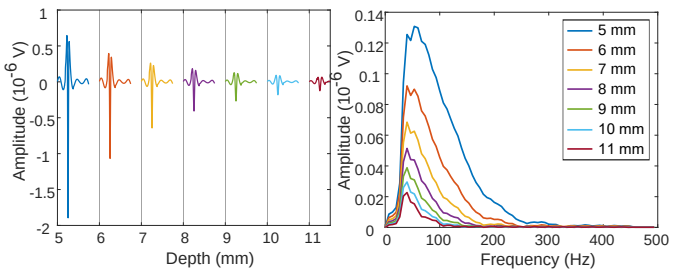

(a) (b)

Fig. 10. Time and frequency domain images of MUAPs with the MU located at different subcutaneous depths.

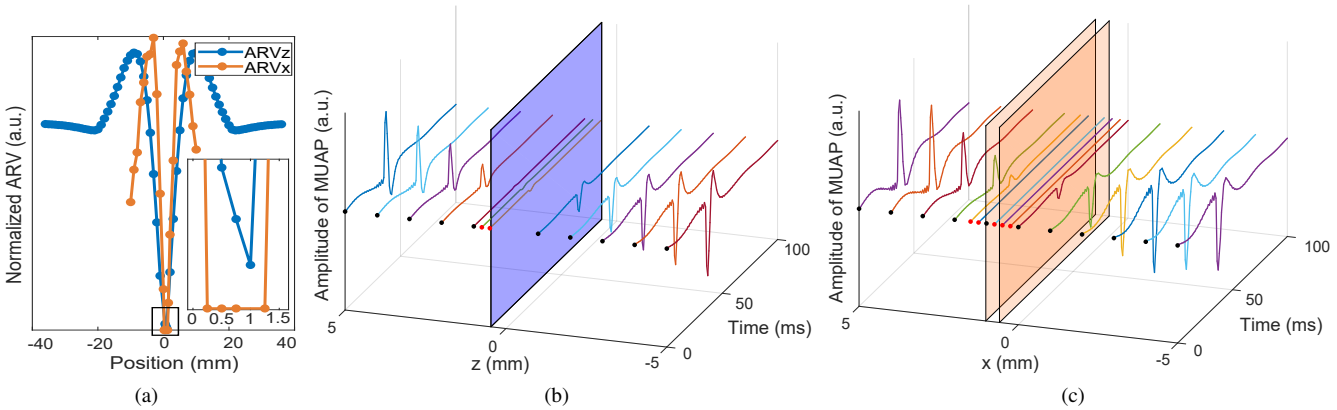

(a) (b) (c)

Fig. 11. Normalized ARVs and scan images of differential signals in the z- and x-axis directions. The scan ranges in the z- and x-axis directions are $[-36, 36]$ and $[-10, 10]$ mm, respectively. (a) The minimum values of ARVs occur at $z = 1$ mm and $x = 0.25$ to 1.25 mm. (b) The potentials with phase reversal occur at $z = 0.75$ and 1 mm. (c) The potentials with phase reversal occur at $x = 0$ and 1.5 mm.

3) The electrode location: Fig. 11a shows the normalized ARV values along the z- and x-axis directions, respectively. The minimum values of ARVs occur at $z = 1$ mm and $x = 0.25$ to 1.25 mm. Figs. 11b and 11c show the waveforms of MUAP along the z- and x-axis directions, respectively. The ranges between the two planes are where the innervation zone and the MU territory are located. Note that due to the small extent of the innervation zone, the two blue planes cannot be seen unless the image is enlarged. The potentials with phase reversal occur at $z = 0.75$ and 1 mm and $x = 0$ and 1.5 mm. Therefore, the position of the innervation zone is in the range of $(0.375, 0.5)$ mm, the position of the MU territory is in the range of $(0, 1.5)$ mm, and the position of the MU territory center is in the range of $(0.214, 1.286)$ mm. The observed results are consistent with the locations of the innervation zone and MU territory. Scan positions are indicated by the black dots spaced 1 mm apart. To locate the positions of the innervation zone and MU territory precisely, the scan positions can be further refined with increased spatial resolution, as the red dots shown in the plots. Moving away from the innervation zone, the ARV value first increases, then decreases, and finally remains stable. In the direction away from the MU territory, the ARV value first becomes larger and then smaller. The difference between adjacent ARVs reduces. The position of the maximum value of ARV is the optimal electrode location, and therefore, the signal-to-noise ratio is high.

C. Electrode Experiment for Elbow Joint Angle Estimation

Based on the simulation results of electrodes in Section III-B and the detailed discussion in Section IV, the size of a single micro-needle electrode is $a_l = b_l = 2.5$ mm, and there are 4×4 micro-needles with a height of 230 μm and a spacing of $e_p = 0.625$ mm. The inter-electrode distance is $e = 6$ mm. As shown in Fig. 6, to achieve consistent coverage with the wet electrode, the high-density micro-needle electrode array introduced four differential channels along the muscle direction, denoted as Ch1, Ch2, Ch3, and Ch4 from proximal to distal. Five different BPNNs were modeled for each channel (Ch1, Ch2, Ch3, Ch4, and Wet). To further evaluate the performance of electrode space utilization, another

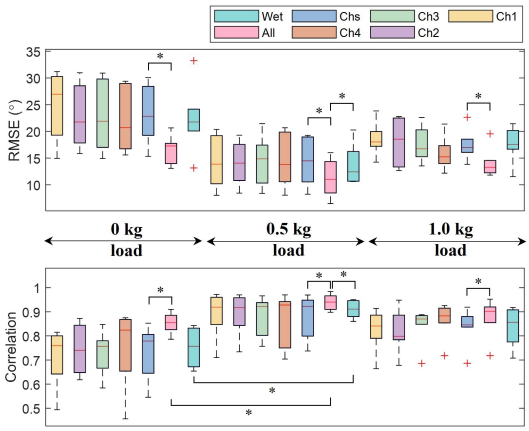

Fig. 12. The overall correlation and RMSE results of the single-channel and all-channel methods under three loads. $*$, $p < 0.05$.

BPNN was modeled using the data of all channels of the high-density micro-needle electrode array (All).

The overall estimation results of the single-channel and all-channel methods under three loads are summarized in Fig. 12. The correlation and RMSE are averaged across all subjects and trials. Chs presents the average single-channel estimation result of the high-density micro-needle electrode array. Wilcoxon rank sum test was performed on the two factors (the method and load). There was no significant difference between the single-channel estimation of the high-density micro-needle electrode array ($p > 0.05$). The single-channel estimation of the high-density micro-needle electrode array was comparable to that of the wet electrode at any load ($p > 0.05$), but lower than the all-channel estimation of the high-density micro-needle electrode array ($p < 0.05$). The all-channel method of the high-density micro-needle electrode array achieved the smallest RMSEs and the highest correlations under 0.5 kg load ($p < 0.05$). The load variation had an essential influence on the performance of angle estimation. The 0.5 kg load showed a better correlation than the 0 kg load for the all-channel high-density micro-needle electrode array and the wet electrode ($p < 0.05$). As shown in Tables S2, S3, and S4 in the supplementary material, the average improvement in the correlation of the high-density micro-needle electrode

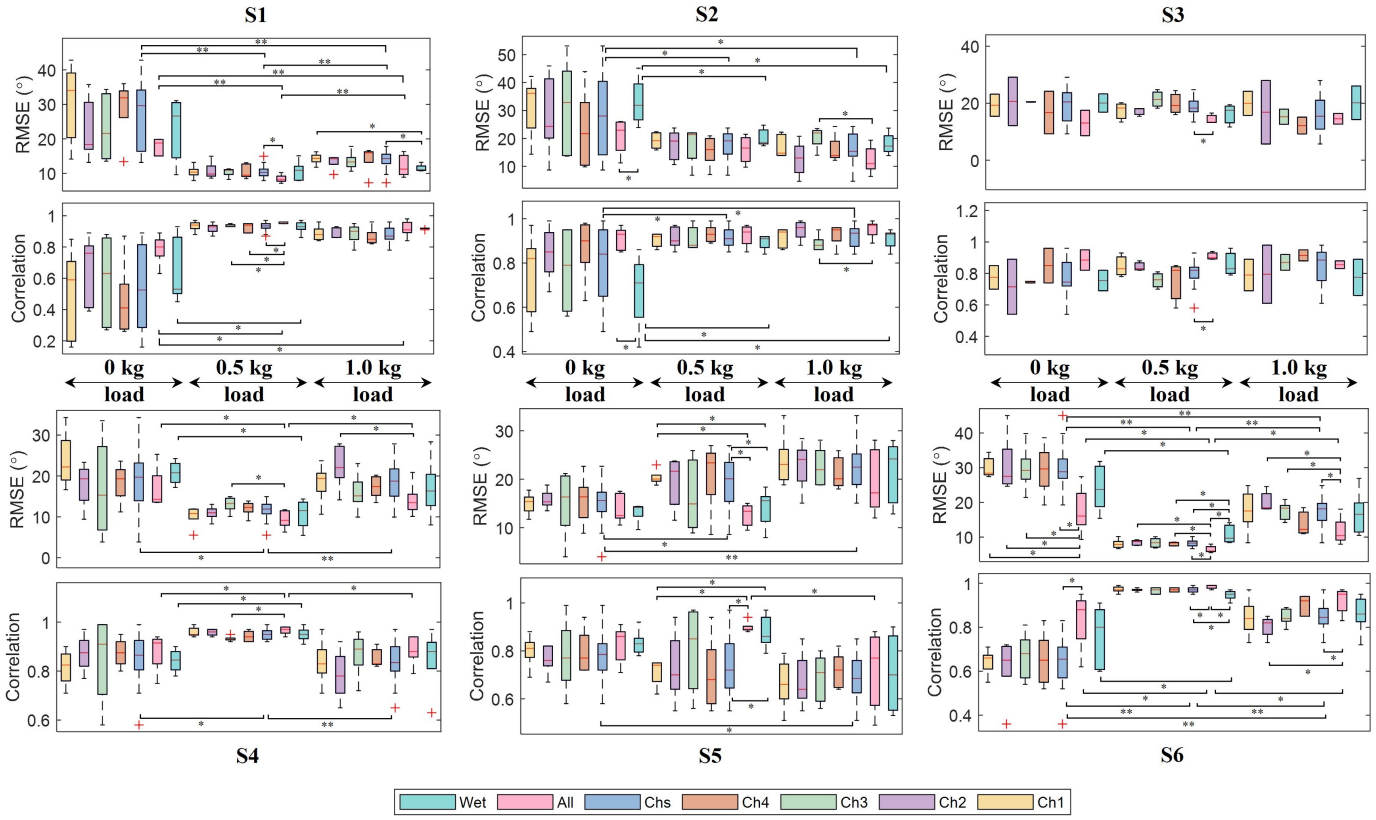

Fig. 13. The correlation and RMSE results of the single-channel and all-channel methods under three loads for each subject. $*$, $p < 0.05$. $**$, $p < 0.01$.

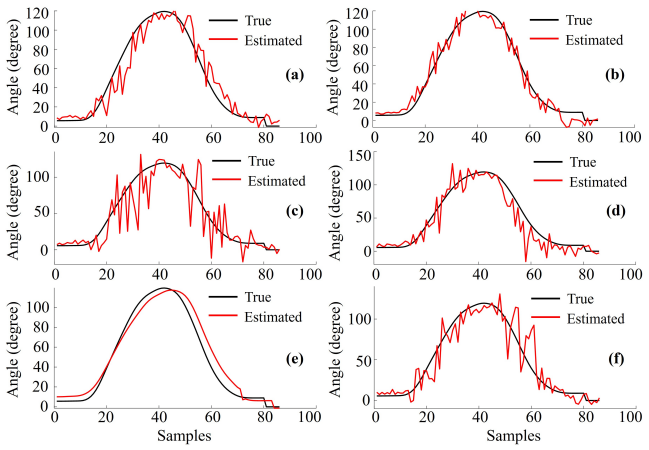

Fig. 14. Comparison of the estimated elbow joint angle (red) with the measured angle (black) under 0.5 kg load for subject S2. (a) Ch1. (b) Ch2. (c) Ch3. (d) Ch4. (e) All. (f) Wet.

array with high space utilization (All-method) under 3 loads is 14.74%, 3.33%, and 4.63%, and the average improvement in the RMSE is 22.35%, 19.11%, and 18.03%. On average, the correlation and RMSE are 7.56% and 19.83% better than those of the wet electrode, respectively.

The estimation results of the single-channel and all-channel methods under three loads for each subject are shown in Fig. 13. The correlation and RMSE are averaged across trials. The load variation had a more significant influence on the performance of angle estimation for individual subjects ($p < 0.01$), such as subject S1. The RMSE comparison of the single-channel method of the high-density micro-needle electrode array with the all-channel method under three loads for subject S6 showed that the performance between channels varied with the load. Fig. 14 shows the estimated angles using each of the six methods under 0.5 kg load for subject S2 compared with the measured values. The correlation is 0.96, 0.98, 0.87, 0.95, 0.98, and 0.93, and the RMSE is 12.42°, 8.25°, 22.34°, 14.92°, 8.66°, and 16.37° from (a) to (f). The estimations are better than those of the wet electrode except for Ch3. The all-channel method estimates smoother angles. Overall, the effectiveness of the high-density micro-needle electrode array and its configuration was verified by experiments.

IV. Discussion

In addition to various complex properties such as the fiber orientation, location, size, and anisotropy of tissues, the muscle fiber number also hinders further exploration of sEMG. Since one MU may be composed of hundreds or thousands of muscle fibers, the simulation costs of MUAP, sEMG, and HD-sEMG are high. In our method, the SFAP only needs to be calculated once for each MU band instead of calculating SFAPs at each time for all muscle fibers. As shown in Table II, the computation time of the MUAP with and without simplification is 30.3 ± 15.8 s and 123.3 ± 9.7 s, and the computation time of the sEMG is 136.3 ± 11.5 s and 3929.5 ± 544.2 s, respectively. The simplified computational method reduces the computation time of an 8×8 HD-sEMG from more than 1 hour to 10 mins and achieves a six-fold reduction compared with the state-of-the-art. Therefore, compared with the traditional model

without simplification, the proposed model greatly improves the simulation efficiency, enabling a large number of muscle fibers to be simulated with very low computational costs.

Based on the fact that MU territories and muscle fibers are uniformly distributed, we developed the NJA algorithm for the generation of uniformly distributed points. The shapes of the muscle and MU territories are assumed to be circular, and this algorithm can be extended to a variety of physiological shapes. As shown in Fig. 7, the NJA algorithm creates highly accurate uniform distribution. The quantitative analysis of the muscle fiber number in each band shows that the NJA algorithm is able to generate the desired number of muscle fibers according to the area and the desired fiber density, which also enables the proposed simplified MUAP computational method.

Fig. 8 demonstrates the ARVs of the same MU measured by electrodes of different sizes. The normalized ARV values measured by electrodes with a size not greater than 3×3 mm are approximately equal to 1, which presents that a small-size electrode can be regarded as a point. As the electrode size increases, the normalized ARV values deviate from 1, suggesting that the potentials in the interval where the distance difference between the electrode and the MU is small are not much different. This observation allows us to realize the simplified model of sEMG, such as the method of the macro-scale motor unit electrical source mentioned in [28] and the notion of the isopotential layer borrowed in this study and [20], to save the computational cost and speed up the calculation.

The average of the non-point electrode potential (see the transfer function in [22]) and the inter-electrode distance (see Fig. 9) both bring a low-pass filtering effect. Therefore, the larger the electrode size and inter-electrode distance, the better the noise suppression and the higher the signal-to-noise ratio, but the spatial sampling frequency is also reduced. On the contrary, the smaller the size, the lower the signal-to-noise ratio, and the more easily the signal is distorted. Therefore, it is recommended to design micro-needle electrodes to expand the area of small electrodes without affecting the spatial sampling frequency. This design not only increases the signal-to-noise ratio but also overcomes the insulation problem of the skin stratum corneum [22]. Small micro-needle electrodes with sizes $a_l, b_l \leq 3$ mm, pin-to-pin distances $e_p \leq 1.25$ mm, and inter-electrode distances $e \leq 6$ mm are recommended, as shown in Fig. 8 and Fig. 9. The conclusion of electrode parameters is similar to that of the studies in [22], [23]. From this viewpoint, most of the sEMG electrodes commonly used do not meet such a design [23].

Fig. 10 simulates the signal characteristics when the MU is at different subcutaneous depths, revealing differences in amplitude and frequency content. The detection volume is mainly derived from SFAPs within 10 mm from the electrode, which is in a similar range to the detection depth estimated by previous analytical models in [23], [27]. The measured signal is only the active signal of the muscle surface, so it is called the sEMG. The potentials generated during source conduction along the muscle fiber and extinction at the tendon diffuse across the skin surface. The signals measured by electrodes may be mixed with contributions from sources of other muscles, a phenomenon known as crosstalk. Although crosstalk is unavoidable, to ensure the purity of the target signal, it is necessary to reduce the interfering signal as much as possible. The simple approach is to place the electrodes in the middle of the muscle belly away from the innervation zone. In addition, the border of the HD-sEMG sensor should be no less than 10 mm away from the muscle border, which defines its maximum limit of size.

There are still limitations to be overcome in the future. More visualization techniques, such as ultrasound and diffusion tensor imaging, are required to improve the anatomical and physiological accuracy of the model to present a subject-specific model. Moreover, obtaining simulations of the HD-sEMG during dynamic contraction is attractive for many applications.

In Section III-C, we designed a high-density micro-needle electrode array based on simulation results for the sEMG measurement of the upper-limb exoskeleton. Although the advantages of micro-needle electrodes for long-term sEMG monitoring without skin preparation are popular in the literature [5], [7], this work focuses on high density, high spatial resolution, and high space utilization. The experimental results show that the rigorously configured micro-needle electrode can match or even outperform the wet electrode (see the RMSE comparison of Ch4 under 0.5 kg load for subject S6), especially the multi-channel array ($p < 0.05$). However, the performance of high-density electrode array is susceptible to interference from bad channels, such as Ch3 in Fig. 14. The estimation accuracy can be maximized by screening the channels (combination and removal), and it will be significantly better than the traditional single-channel estimation. We also observe that the estimation performance with load is superior to that without load ($p < 0.05$) [41]. Moreover, the dominant channel in the high-density electrode array varies under different loads. These are mainly due to the different activation patterns of muscles, with different numbers and positions of MUs being recruited and discharged.

The high-density electrode array captures spatial information and thus has greater potential for practical and clinical applications. The performance of the neural-driven approach is superior to the traditional sEMG-driven approach, especially during fast movements [40]. In the future, we will attempt to decode MUAPs from HD-sEMG recorded by the proposed high-density micro-needle electrode array for more robust and precise control of exoskeleton robots.

V. Conclusion

Understanding muscle composition, anatomical and physiological properties, and the process of sEMG generation is critical for extracting accurate motion and intention information from sEMG signals. This work presented modifications to the locations of MUs and muscle fibers and the geometry of motor end-plates for HD-sEMG recordings. Based on the modifications, a simplified computational method was proposed to improve the simulation efficiency. The 2D high-density micro-needle electrode configuration was carried out using the neuromuscular analytical model for HD-sEMG. The application of the configured micro-needle electrode array in

elbow joint angle estimation was demonstrated for verification and comparison. The model can be used as an effective tool for the development and analysis of HD-sEMG signals, and the developed 2D high-density micro-needle electrode array shows promising potential for practical applications.

REFERENCES

[1] Z. Tang, H. Yu, and S. Cang, "Impact of load variation on joint angle estimation from surface EMG signals," *IEEE Trans. Neural Syst. Rehabilitation Eng.*, vol. 24, no. 12, pp. 1342–1350, 2015.

[2] Z. Tang, H. Yu, H. Yang, L. Zhang, and L. Zhang, "Effect of velocity and acceleration in joint angle estimation for an EMG-Based upper-limb exoskeleton control," *Comput. Biol. Med.*, vol. 141, p. 105156, 2022.

[3] Y. Gu, J. Li, W. Fan, N. Zhang, X. Zhang, and T. Liu, "A Wearable Monitoring System and Multi-Index Fusion Approach for Adaptability Assessment of Prosthetic Hands," *IEEE Trans. Instrum. Meas.*, 2023.

[4] D. Farina, I. Vujaklija, M. Sartori, T. Kapelner, F. Negro, N. Jiang, K. Bergmeister, A. Andalib, J. Principe, and O. C. Aszmann, "Man/machine interface based on the discharge timings of spinal motor neurons after targeted muscle reinnervation," *Nat. biomed. eng.*, vol. 1, no. 2, p. 0025, 2017.

[5] H. Ji, M. Wang, Y. Wang, Z. Wang, Y. Ma, L. Liu, H. Zhou, Z. Xu, X. Wang, Y. Chen *et al.*, "Skin-integrated, biocompatible, and stretchable silicon microneedle electrode for long-term EMG monitoring in motion scenario," *npj Flex. Electron.*, vol. 7, no. 1, p. 46, 2023.

[6] H.-L. Peng, J.-Q. Liu, Y.-Z. Dong, B. Yang, X. Chen, and C.-S. Yang, "Parylene-based flexible dry electrode for bioptential recording," *Sens. Actuators, B*, vol. 231, pp. 1–11, 2016.

[7] L. Ren, B. Liu, W. Zhou, and L. Jiang, "A mini review of microneedle array electrode for bio-signal recording: a review," *IEEE Sen. J.*, vol. 20, no. 2, pp. 577–590, 2019.

[8] H. Jeong, J. Feng, and J. Kim, "2.5 D laser-cutting-based customized fabrication of long-term wearable textile sEMG sensor: From design to intention recognition," *IEEE Robot. Automat. Lett.*, vol. 7, no. 4, pp. 10 367–10 374, 2022.

[9] H.-R. Lim, H. S. Kim, R. Qazi, Y.-T. Kwon, J.-W. Jeong, and W.-H. Yeo, "Advanced soft materials, sensor integrations, and applications of wearable flexible hybrid electronics in healthcare, energy, and environment," *Adv. Mater.*, vol. 32, no. 15, p. 1901924, 2020.

[10] F. S. Ayachi, S. Boudaoud, and C. Marque, "Evaluation of muscle force classification using shape analysis of the sEMG probability density function: a simulation study," *Med. biol. eng. comput.*, vol. 52, pp. 673–684, 2014.

[11] M. Al Harrach, S. Boudaoud, V. Carriou, J. Laforet, A. J. Letocart, J.-F. Grosset, and F. Marin, "Investigation of the HD-sEMG probability density function shapes with varying muscle force using data fusion and shape descriptors," *Comput. Biol. Med.*, vol. 89, pp. 44–58, 2017.

[12] A. J. Young, L. J. Hargrove, and T. A. Kuiken, "Improving myoelectric pattern recognition robustness to electrode shift by changing interelectrode distance and electrode configuration," *IEEE Trans. Biomed. Eng.*, vol. 59, no. 3, pp. 645–652, 2011.

[13] Y. Fang, W. Guo, and X. Sheng, "An Electrode Configuration Framework for sEMG-Based Gesture Recognition with Muscle-matched Layouts," *IEEE Trans. Instrum. Meas.*, 2023.

[14] H. J. Hermens, B. Freriks, C. Disselhorst-Klug, and G. Rau, "Development of recommendations for SEMG sensors and sensor placement procedures," *J. Electromyogr. Kinesiology*, vol. 10, no. 5, pp. 361–374, 2000.

[15] V. Carriou, S. Boudaoud, J. Laforet, and F. S. Ayachi, "Fast generation model of high density surface EMG signals in a cylindrical conductor volume," *Comput. Biol. Med.*, vol. 74, pp. 54–68, 2016.

[16] M. Al Harrach, V. Carriou, S. Boudaoud, J. Laforet, and F. Marin, "Analysis of the sEMG/force relationship using HD-sEMG technique and data fusion: A simulation study," *Comput. Biol. Med.*, vol. 83, pp. 34–47, 2017.

[17] S. Ma, B. Lv, C. Lin, X. Sheng, and X. Zhu, "EMG signal filtering based on variational mode decomposition and sub-band thresholding," *IEEE J. Biomed. Health. Inf.*, vol. 25, no. 1, pp. 47–58, 2020.

[18] E. Stålberg and L. Karlsson, "Simulation of EMG in pathological situations," *Clin. Neurophysiol.*, vol. 112, no. 5, pp. 869–878, 2001.

[19] G. V. Dimitrov, C. Disselhorst-Klug, N. A. Dimitrova, E. Schulte, and G. Rau, "Simulation analysis of the ability of different types of multi-electrodes to increase selectivity of detection and to reduce cross-talk," *J. Electromyogr. Kinesiology*, vol. 13, no. 2, pp. 125–138, 2003.

[20] A. J. Fuglevand, D. A. Winter, A. E. Patla, and D. Stashuk, "Detection of motor unit action potentials with surface electrodes: influence of electrode size and spacing," *Biol. Cybern.*, vol. 67, no. 2, pp. 143–153, 1992.

[21] D. Farina and R. Merletti, "A novel approach for precise simulation of the EMG signal detected by surface electrodes," *IEEE Trans. Biomed. Eng.*, vol. 48, no. 6, pp. 637–646, 2001.

[22] B. Afsharipour, S. Soedirdjo, and R. Merletti, "Two-dimensional surface EMG: The effects of electrode size, interelectrode distance and image truncation," *Biomed. Signal Process. Control*, vol. 49, pp. 298–307, 2019.

[23] R. Merletti and S. Muceli, "Tutorial. Surface EMG detection in space and time: Best practices," *J. Electromyogr. Kinesiology*, vol. 49, p. 102363, 2019.

[24] L. Mesin, M. Joubert, T. Hanekom, R. Merletti, and D. Farina, "A finite element model for describing the effect of muscle shortening on surface EMG," *IEEE Trans. Biomed. Eng.*, vol. 53, no. 4, pp. 593–600, 2006.

[25] S. Nandedkar *et al.*, "Simulation of single muscle fibre action potentials," *Med. Biol. Eng. Comput.*, vol. 21, no. 2, pp. 158–165, 1983.

[26] A. Konstantin, T. Yu, E. Le Carpentier, Y. Aoustin, and D. Farina, "Simulation of motor unit action potential recordings from intramuscular multichannel scanning electrodes," *IEEE Trans. Biomed. Eng.*, vol. 67, no. 7, pp. 2005–2014, 2019.

[27] D. Pereira Botelho, K. Curran, and M. M. Lowery, "Anatomically accurate model of EMG during index finger flexion and abduction derived from diffusion tensor imaging," *PLoS Comput. Biol.*, vol. 15, no. 8, p. e1007267, 2019.

[28] V. Carriou, S. Boudaoud, and J. Laforet, "Speedup computation of HD-sEMG signals using a motor unit-specific electrical source model," *Med. Biol. Eng. Comput.*, vol. 56, no. 8, pp. 1459–1473, 2018.

[29] F. Buchthal, C. Guld, and P. Rosenfalck, "Multielectrode study of the territory of a motor unit," *Acta Physiol. Scand.*, vol. 39, no. 1, pp. 83–104, 1957.

[30] I. Gath and E. Stålberg, "On the measurement of fibre density in human muscles," *Electroencephalogr. Clin. Neurophysiol.*, vol. 54, no. 6, pp. 699–706, 1982.

[31] A. J. Fuglevand, D. A. Winter, and A. E. Patla, "Models of recruitment and rate coding organization in motor-unit pools," *J. Neurophysiol.*, vol. 70, no. 6, pp. 2470–2488, 1993.

[32] S. Ma, C. Chen, J. Zhao, D. Han, X. Sheng, D. Farina, and X. Zhu, "Analytical modelling of surface EMG signals generated by curvilinear fibers with approximate conductivity tensor," *IEEE Trans. Biomed. Eng.*, vol. 69, no. 3, pp. 1052–1062, 2021.

[33] G. V. Dimitrov and N. A. Dimitrova, "Precise and fast calculation of the motor unit potentials detected by a point and rectangular plate electrode," *Med. Eng. Phys.*, vol. 20, no. 5, pp. 374–381, 1998.

[34] P. Rosenfalck, "Intra-and extracellular potential fields of active nerve and muscle fibres," *Acta Physiol. Scand.*, vol. 321, 1969.

[35] J. Duchene and J.-Y. Hogrel, "A model of EMG generation," *IEEE Trans. Biomed. Eng.*, vol. 47, no. 2, pp. 192–201, 2000.

[36] A. Hamilton-Wright and D. W. Stashuk, "Physiologically based simulation of clinical EMG signals," *IEEE Trans. Biomed. Eng.*, vol. 52, no. 2, pp. 171–183, 2005.

[37] T. H. Gootzen, D. F. Stegeman, and A. Van Oosterom, "Finite limb dimensions and finite muscle length in a model for the generation of electromyographic signals," *Electroencephalogr. Clin. Neurophysiol./Evoked Potentials Section*, vol. 81, no. 2, pp. 152–162, 1991.

[38] J. Navallas *et al.*, "Studying motor end-plate topography by means of scanning-electromyography," *Clin. Neurophysiol.*, vol. 120, no. 7, pp. 1335–1341, 2009.

[39] A. Rainoldi, M. Nazzaro, R. Merletti, D. Farina, I. Caruso, and S. Gaudenti, "Geometrical factors in surface EMG of the vastus medialis and lateralis muscles," *J. Electromyogr. Kinesiology*, vol. 10, no. 5, pp. 327–336, 2000.

[40] C. Dai and X. Hu, "Finger joint angle estimation based on motoneuron discharge activities," *IEEE J. Biomed. Health. Inf.*, vol. 24, no. 3, pp. 760–767, 2019.

[41] C. Shen, Z. Pei, W. Chen, Z. Li, J. Wang, J. Zhang, and J. Chen, "STMI: Stiffness Estimation Method Based on sEMG-Driven Model for Elbow Joint," *IEEE Trans. Instrum. Meas.*, 2023.